JOURNAL OF PETROLOGY | VOLUME 49 | NUMBER 9 | PAGES 1647–1665 | 2008 | doi:10.1093/petrology/egn041

Experiments and Models Bearing on the Role of Chromite as a Collector of Platinum Group Minerals by Local Reduction

CRAIG S. FINNIGAN[1], JAMES M. BRENAN[1]*, JAMES E. MUNGALL[1] AND W. F. McDONOUGH[2]

[1]DEPARTMENT OF GEOLOGY, UNIVERSITY OF TORONTO, ONTARIO, CANADA, M5S 3B1

[2]DEPARTMENT OF GEOLOGY, UNIVERSITY OF MARYLAND, COLLEGE PARK, MD 20742, USA

RECEIVED MAY 19, 2006; ACCEPTED AUGUST 15, 2008
ADVANCE ACCESS PUBLICATION SEPTEMBER 6, 2008

Chromite is widely recognized to act as a collector for platinum group elements (PGE), which tend to be observed as discrete grains of platinum group minerals included within magmatic chromite grains. In the course of experiments involving the re-equilibration or growth of chromite and Cr-spinel in molten silicate, we observe that platinum group minerals (PGM; including metal alloys and laurite) form at the mineral–melt interface. The formation of PGM to the extent observed requires a mechanism involving sustained transport of PGE from a source within the experiment to the site of deposition. We propose that the driving force for this process is a redox gradient developed in response to mineral growth or re-equilibration with the surrounding melt. The mechanism is local reduction within the mineral–melt interfacial region as a consequence of the selective uptake of trivalent Cr and Fe from the melt by spinel relative to the divalent species. We have modeled the transient perturbation of fO_2 *in a compositional boundary layer melt around spinel for both crystal growth and diffusive re-equilibration of mineral and melt. We find that metal solubilities decrease by several per cent in the silicate melt at the melt–crystal interface during crystal growth, providing the driving force for PGM formation. In magmas that are saturated with PGM, as a result of falling temperature and oxygen fugacity during spinel crystallization, nucleation of PGM will be impeded by interfacial tension everywhere except in the reduced boundary layer around spinel crystals. The resulting concentration and trapping of alloy particles in the growing chromite crystals can produce apparent bulk chromite/melt partition coefficients exceeding 20 even if there is no solid solution of PGE in the chromite. The introduction of spinel grains, initially equilibrated with a mafic magma, into a more primitive magma, with higher Cr/Al, would lead to disequilibrium between chromite and melt. The perturbation of* fO_2 *in the compositional boundary layer surrounding a chromite xenocryst would exceed 0·1 log unit, leading to local reduction of alloy solubility of the order of 13–18%. A small number of spinel xenocrysts could serve as collection sites for all of the excess PGE in the magma, leading to the eventual observation that a few chromite crystals contain many PGM inclusions, whereas the rest of the chromite population may be relatively free of PGM.*

KEY WORDS: *platinum group minerals; platinum group elements; chromite; alloys*

INTRODUCTION

Platinum group minerals (PGM), most commonly Pt–Fe and Os–Ir alloys and laurite, frequently occur as inclusions within chromite (Legendre & Augé, 1986; Talkington & Lipin, 1986; Merkle, 1992; Garuti *et al.*, 1999; Gervilla & Kojonen, 2002; Zaccarini *et al.*, 2002). Inclusions are generally sub-millimetre in size but may also occur on the nanometre scale as inferred from *in situ* analysis by laser ablation inductively coupled plasma mass spectrometry (LA-ICP-MS) (e.g. Ballhaus & Sylvester, 2000). A variety of observations suggest that the PGM formed at high temperature and were entrapped at the time of chromite crystallization (Legendre & Augé, 1986; Peck *et al.*, 1992; Zaccarini *et al.*, 2002). Experimental studies show that laurite and Ru–Os–Ir alloys are stable at chromian-spinel liquidus temperatures over some range of fS_2, provided the system is undersaturated with sulfide liquid, indicating

*Corresponding author. E-mail: brenan@geology.utoronto.ca

that PGM inclusions in chromian spinel can be interpreted as a primary magmatic texture (Brenan & Andrews, 2001; Andrews & Brenan, 2002; Bockrath *et al.*, 2004). As a possible mechanism for alloy formation, Capobianco *et al.* (1994) have suggested that PGM precipitate in response to disproportionation reactions that occur in the melt as a result of the uptake of high concentrations of some platinum group elements (PGE) as a dissolved component in the chromite lattice. Alloy grains formed by this process, and included in the crystal, may subsequently coarsen by exsolution during cooling (e.g. Gijbels *et al.*, 1974). Ballhaus *et al.* (2006) suggested that Ir and Ru alloys have a propensity for heterogeneous nucleation on chromite surfaces. Hiemstra (1979) emphasized the role of chromite as an early 'collector' for very small grains of PGM, thereby enhancing their settling rate, and efficient separation from the magma.

Apart from igneous crystallization, other processes have been invoked to explain chromite-hosted PGM. The occurrence of hydrous and halogen-rich phases in some chromitites has led workers to suggest that PGM formation is the result of deposition from a hydromagmatic fluid, which has scavenged PGE from the underlying pile of crystallizing magma (Mathez, 1995; Boudreau & Meurer, 1999). The PGE in chromitites may be locally derived from interstitial sulfide. Desulfidation following Fe loss to chromite could liberate the PGE (Naldrett & Lehmann, 1988; Maier & Barnes, 1999; Maier *et al.*, 2003; Peregoedova *et al.*, 2004). The problem with this theory is that the partitioning of PGE from silicate melt into sulfide melt is not expected to produce the extreme fractionation of IPGE (Ir, Ru, Os) that is observed in many chromitites. Because inclusions found in natural samples are generally IPGE enriched, early saturation of PGE alloys or sulfides at the magmatic stage is a mechanism to explain the relative IPGE depletion observed in mafic or ultramafic rock suites (e.g. Barnes *et al.*, 1985; Legendre & Augé, 1986; Fleet & Stone, 1991; Tredoux *et al.*, 1995; Maier & Barnes, 1999; Puchtel & Humayen, 2001; Puchtel *et al.*, 2004). Establishing the timing of PGM formation is clearly of importance to understanding the geochemistry of the PGE in mafic igneous rocks.

Mungall (2002) presented a model in which magmas that are close to PGE saturation will precipitate PGM as a result of kinetically controlled local reduction in the melt related to chromite growth. Because the Fe^{3+}/Fe^{2+} and Cr^{3+}/Cr^{2+} ratios in chromite exceed those of the melt, the relative abundance of reduced species is elevated in the melt adjacent to the crystal. This creates a local reduction in fO_2, which in turn lowers the solubility of the PGE in the melt (Ertel *et al.*, 1999; Borisov & Palme, 2000; Borisov & Walker, 2000). The rationale for the experimental methods described in this paper stems from our past work on chromite–melt partitioning (i.e. Sattari *et al.*, 2002), in which we encountered difficulties in growing large, inclusion-free chromites. As a result, we devised a new method for measuring chromite–melt partition coefficients, in which the margins of natural, nominally PGE-free chromite crystals are equilibrated with PGE-bearing melt by diffusive exchange (the partitioning results will be reported elsewhere). In the course of running these experiments, we encountered textures that we believe are explicable in the context of Mungall's (2002) model.

EXPERIMENTAL TECHNIQUES

Sulfur-free experiments

Sulfur-free experiments were performed in a vertical tube gas mixing furnace in which fO_2 was controlled using mixtures of CO and CO_2, and confirmed before and after each run using a Y-doped zirconia oxygen sensor (Australian Oxytrol Systems, Ltd). Most gas-mixing experiments were carried out at 1400°C, with the exception of four experiments that were held isothermally, then cooled 30°C over 1 h. Temperatures were monitored using a type S thermocouple. Experiments were performed at log fO_2 ranging from −2·5 to −7·3, corresponding to FMQ +3·8 to −1·0 (where FMQ is the fayalite–magnetite–quartz buffer) at 1400°C, for durations of 3–336 h. The proportions of CO_2 and CO were kept constant in the cooling experiments, as this allows the fO_2 of the sample to decrease by 0·3 log units over the cooling interval, which is in exact accord with the change in the fO_2 of the FMQ buffer. As such, values of ΔFMQ remain constant. Minerals used in experiments were obtained from two sources: (1) crystals separated from a massive chromitite sample from New Caledonia (Royal Ontario Museum reference number M36331; hereafter N-C chromite); (2) a single Al-rich spinel megacryst from the Roberts-Victor mine, Republic of South Africa (courtesy of Dr Dan Schulze; hereafter R-V spinel). The melt employed in this study is a Tertiary-age microporphyritic alkali olivine basalt from East Greenland (Hogg *et al.*, 1989). The compositions of these materials are presented in Table 1. The basalt starting material was first finely powdered in a chrome-steel swing mill to a grain size of $< 20\,\mu m$, then calcined at 1000°C in air for 12 h. N-C chromite or R-V spinel was added to experiments using one of three methods. In most experiments, basalt powder was mixed with polyvinyl alcohol (PVA) and packed around a 0·5 mm × 1 mm × 1 mm mineral wafer. Some experiments used a mixture of PVA, basalt and minerals that were ground and sieved to a specific size fraction (35–40 or 75–90 μm). We also employed a hybrid technique in which both a mineral slab and a sieved size fraction were added. The sample configuration for slab-bearing experiments is shown in Fig. 1a; experiments including the sieved fraction used a similar geometry. Each sample was bonded to a wire loop, which was hung from the end of a silica rod during the experiment.

Table 1: Composition of starting materials

	New Caledonia $n=32$	Roberts Victor $n=10$	Greenland basalt*
wt %			
SiO_2			43·49
TiO_2	0·13(0·02)	0·13(0·02)	4·45
Al_2O_3	10·68(0·10)	62·44(0·34)	6·82
Fe_2O_3	5·48(0·23)†	4·23(0·47)†	—
FeO	9·90(0·64)	10·0(0·47)	13·9
MnO	0·15(0·03)	0·10(0·02)	0·16
MgO	15·44(0·39)	20·38(0·37)	14·81
CaO	n.a.	n.a.	9·99
Na_2O	n.a.	n.a.	1·6
K_2O	n.a.	n.a.	1·18
P_2O_5	n.a.	n.a.	0·54
Cr_2O_3	58·63(0·45)	2·10(0·04)	0·129
NiO	0·18(0·02)	0·53(0·01)	0·013
LOI	n.a.	n.a.	1·91
Total	100·58	99·92	99·06
PGE abundances (ppm)			
	$n=3$	$n=3$	
Os	0·048(0·015)	0·031(0·010)	
Ir	<0·015	0·043(0·008)	
Ru	0·087(0·018)	0·13(0·07)	
Rh	0·029(0·007)	0·049(0·003)	
Pd	<0·080	<0·080	
Pt	<0·04	0·054(0·028)	

*XRF analysis, Hogg *et al.* (1989).
†Calculated from stoichiometry using the method of Barnes & Roeder (2001).
LOI, loss on ignition; n.a., not analyzed.

Experiments involving Pt, Rh, Ir and Pd used loop wires made from the pure metal or metal alloy (Pt/Rh). Os, Ru and Au were added to experiments in the powdered form, and samples were suspended using Pd wire, which is largely immiscible with these metals. Specific metals or metal combinations used in the experiments are listed in Table 2. Samples were quenched by rapid immersion in a cold water bath situated outside the lower end of the furnace tube.

Sulfur-bearing experiments

To investigate the formation of the PGE sulfide laurite (RuS_2) a sulfur-bearing experiment was carried out using a vacuum-sealed thick-walled (10 mm o.d., 4·1 mm i.d.) fused silica ampoule and the $Ru + RuS_2$ assemblage to buffer the fS_2. The experiment was of the 'dynamic' type, and first held isothermally for 10 h, then cooled 20°C over 1 h. The experiment was prepared by placing a wafer of

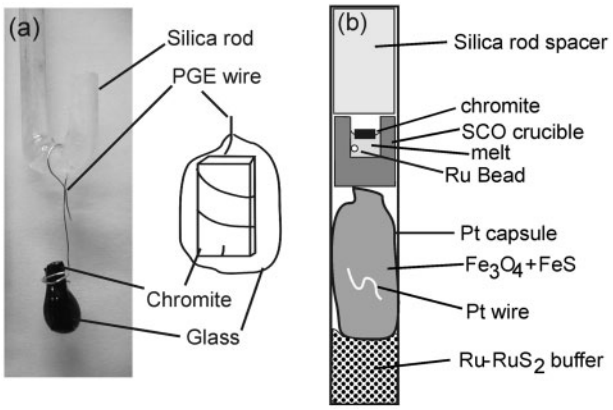

Fig. 1. Configurations for the experiments performed in this study. (a) Photograph and schematic illustration of sample employed in gas-mixing experiments showing the chromite wafer wrapped with a PGE wire encased in melt. (b) Schematic illustration of sulfur-bearing experiment in which the sample is encapsulated in an evacuated silica ampoule with the fS_2 buffered by the Ru–RuS_2 assemblage and the fO_2 estimated from the Fe content of a Pt wire in contact with magnetite.

N-C chromite in the bottom of a crucible made from a San Carlos olivine megacryst; the crucible was then backfilled with basalt, and a bead of high-purity Ru was placed into the basalt powder (Fig. 1b). The absolute fO_2 was determined after the experiment to be FMQ + 0·9 (log $fO_2 = -7·5$) by measuring the Fe content of a Pt wire packed in magnetite (Kessel *et al.*, 2001), which was contained in a crimped but unwelded Pt capsule placed directly below the sample container. Based on previous reconnaisance experiments, it was determined that some of the magnetite reacts with the sulfur vapor to form FeS melt. As this is an additional sink for S from the buffer, and consumes the magnetite, we limited the extent of this reaction by adding presynthesized FeS powder with the magnetite. The oxygen fugacity was therefore buffered in this experiment by the presence of the magnetite + sulfide melt. The experiment was carried out in a bottom-loading box furnace in which the silica tube was placed upright in an alumina crucible on the furnace hearthplate, and temperature was monitored using a calibrated type S thermocouple located immediately above the sample. The experiment was terminated by lowering the furnace floor, then plunging the sample into cold water. The presence of both metal and sulfide phases in the buffering assemblage was confirmed after the experiment by X-ray diffraction.

ANALYTICAL TECHNIQUES

Textural and chemical

Run products containing a sieved grain fraction were fractured into pieces whereas those containing wafers were sectioned in half laterally. All material was then mounted in

Table 2: Summary of experiments

Experiment number	Metal mix*	T (°C)	log fO_2	△FMQ	Duration (h)	Spinel	Technique	PGM present
Pt/Rh −2·5 3h	Pt-Rh	1400	−2·5	3·8	3	New Cal	slab	yes
Rh −2·5 5h	Rh	1400	−2·5	3·8	5	New Cal	slab and 35–40 μm	yes
Rh −2·5 3d	Rh	1400	−2·5	3·8	72	New Cal	slab	yes
Rh −2·5 5d	Rh	1400	−2·5	3·8	120	New Cal	slab	yes
Rh −2·5 7d	Rh	1400	−2·5	3·8	168	New Cal	slab and 35–40 μm	yes
Rh −2·5 14d	Rh	1400	−2·5	3·8	336	New Cal	slab and 35–40 μm	yes
Pd/Ru −2·5b	Pd/Ru	1400	−2·5	3·8	168	New Cal	75–90 μm	yes
Pt/Rh −2·5b	Pt-Rh	1400	−2·5	3·8	168	New Cal	75–90 μm	yes
Pt/Rh −2·5	Pt-Rh	1400	−2·5	3·8	336	New Cal	35–40 μm	No
Pt/Rh −3·8	Pt-Rh	1400	−3·8	2·5	168	New Cal	slab	yes
Pd/Ru −3·8	Pd (Ru)	1400	−3·8	2·5	168	New Cal	slab	yes
Pd/Os/Au −3·8	Pd(Os,Au)	1400	−3·8	2·5	168	New Cal	slab	yes
Pd/Ir/Au −3·8	Pd(Ir,Au)	1400	−3·8	2·5	168	New Cal	slab	yes
Pt/Rh −5	Pt-Rh	1400	−5	1·3	168	New Cal	75–90 μm	yes
Rh −5	Rh	1400	−5	1·3	168	New Cal	slab	yes
Pd/Ru −5	Pd(Ru)	1400	−5	1·3	168	New Cal	slab and 75–90 μm	yes
Pd/Os/Au −5	Pd(Os,Au)	1400	−5	1·3	168	New Cal	slab	yes
Pd/Ir/Au −5·0	Pd(Ir,Au)	1400	−5	1·3	168	New Cal	slab	yes
Ir −7·3 dynamic†	Ir	1400/1370	−7·3	−1	5	Rob Vic	slab	yes
Rh −7·3 dynamic	Rh	1400/1370	−7·3	−1	4	Rob Vic	slab	yes
Ru −7·3 dynamic	Pd(Ru)	1400/1370	−7·3	−1	4	Rob Vic	slab	yes
Os −7·3 dynamic	Pd(Ru)	1400/1370	−7·3	−1	4	Rob Vic	slab	yes
RuS dynamic‡	Ru	1220/1200	−7·5	0·9	11	New Cal	slab	Yes

*Composition of wire loop in gas mixing experiments; other powders added are given in parentheses. Ru powder was used in the RuS dynamic experiment.
†Held isothermally then cooled 20–30°C over 1 h (total run duration reported).
‡log fS_2 calculated to be −1·6 at 1220°C from data of Barin (1995).

epoxy and polished first with 600 grit SiC, followed by 1200 grit SiC and finally 1 μm diamond. One sample (Rh −2·5 3d) was immersed in concentrated HF, which dissolved the silicate glass but left the chromite intact, revealing the distibution of PGE alloys on the chromite surface. Textural characteristics of run products were observed using reflected light and scanning electron microscopy (SEM). The JEOL 840 scanning electron microscope at the University of Toronto was used to obtain backscatter electron and secondary electron images, and phases were characterized chemically using energy dispersive spectroscopy (EDS). Beam conditions were 20–30 kV, 3 nA and a working distance of 30 mm. Quantitative analyses of PGM could not be performed because of their small size.

Major element analyses were performed on both the melt and spinel phases using the Cameca SX50 electron microprobe at the University of Toronto. Beam conditions for glass analysis were 15 kV and 10 nA with a beam diameter of either 1 or 10 μm. Conditions for spinel analysis were 20 kV and 30 nA with a beam focused to a diameter of 1 μm. Standards for glass analyses were natural basalt (Si, Al, Fe, Mg), bustamite (Ca, Mn), albite (Na), titanium oxide (Ti), chromium oxide (Cr), pentlandite (S, Ni) and sanidine (K). Standards for spinel were chromium oxide (Cr), gahnite (Al), magnesium oxide (Mg), haematite (Fe), rhodonite (Mn), titanium oxide (Ti), and pentlandite (Ni). For all analyses raw count rates were converted to concentrations using the ZAF data reduction scheme. The FeO and Fe_2O_3 content of chromites were calculated by stoichiometry after the method of Barnes & Roeder (2001). Parkinson & Arculus (1999) have shown that the uncertainties associated with Fe speciation determined by this method are small for spinels with Fe^{3+}/total Fe >0·4 (corresponding to synthesis at > FMQ + 1), which is the case for most of the experiments reported in this study. To characterize chemical gradients in spinel and glass, analyses were performed perpendicular to the spinel–glass interface. A concern in this approach is that the apparent chromium content of glass close to the chromite–melt interface may be enhanced by beam impingement on the chromite,

or secondary fluoresence. To correct for this, polished faces of chromite and glass fragments were bound together, sectioned and polished, then analyses were made of the glass adjacent to the chromite. A second-order polynomial was fitted to the Cr vs distance data, which were then subtracted from glass analyses adjacent to chromite from experimental run products. It should be noted that this procedure somewhat overestimates the edge effects, as the Cr content at the margins of run-product chromites is about half that of the starting material, which was used to calibrate the correction.

The PGE contents of some run-product glasses, and the chromite starting materials, were determined using the LA-ICP-MS facilities in the Departments of Geology at the University of Maryland and at University of Toronto. Both systems employ a frequency quintupled Nd:YAG laser operating at 213 nm, coupled to either an Element 2 (ThermoElectron) magnetic sector ICP-MS system (Maryland), or a VG PQExcell quadrupole ICP-MS system (Toronto) with He flushing the ablation cell to enhance sensitivity (Eggins *et al.*, 1998). Conditions for laser ablation analyses (e.g. spot size, beam irradiance, repetition rate) of the phases analyzed in this study were optimized for each sample, depending on element concentration and photon-coupling characteristics. Typically, analyses were obtained using a laser repetition rate of 10 Hz and a spot size of 100–200 μm. Factory-supplied time-resolved software was utilized for the acquisition of single analyses. A typical analysis involved 20 s of background acquisition with the ablation cell being flushed with He, followed by laser ablation for 60 s. Analyses were collected in a sequence, with the first and last four spectra acquired on standard reference materials (SRM). SRM employed include NIST 610 silicate glass and 'in house' standard JB-sulfide, a NiS bead containing ~400 ppm of each PGE. Data reduction was performed using either LAMTRACE (Maryland) or GLITTER (Toronto) version 5.3 software package, supplied by Macquarie Research, Ltd. Ablation yields in standard and unknowns were corrected by referencing to the known concentration of an element as determined previously by electron microprobe analyses. Ca was used as the reference element for silicate glass and Ni for spinel; this method also provided precise Ni (in glass) and Cu (glass and spinel) data that in turn were used to correct ablation yields when using the sulfide standard. As a check for interference, element concentrations were determined using multiple isotopes, when possible. The following isotopes were used to determine element concentrations reported in this study: ^{99}Ru, ^{103}Rh, ^{106}Pd, ^{189}Os, ^{193}Ir and ^{194}Pt.

RESULTS

Textural observations

Images of the sulfur-free experiments involving N-C chromite reveal alloy grains 1–10 μm in size attached to the margin of the chromite wafer and projecting into the melt (Fig. 2a–d). The grains are distributed on all chromite surfaces that were in contact with the melt. Some alloy grains show well-developed crystal faces (Fig. 2b and d) with forms consistent with their crystal symmetry. In cases where the chromite appears to have fractured and 'healed' during the experiment, metal grains have become entrapped by the new mineral crystallization. Chromite grains produced in experiments starting with a sieved mineral fraction are generally anhedral in their morphology. Experiments that employed the 75–90 μm sized starting material produced alloy at the chromite–melt interface (Fig. 3a) for all conditions studied, whereas those using a 35–40 μm grain fraction produced alloy in experiments of 168 h duration, but were alloy-free after 336 h (Fig. 3b). Spinels produced during the cooling experiments exhibit a 'vermiform' texture (Roeder *et al.*, 2001) reflecting diffusion-controlled growth. In those experiments, alloys are present at the spinel–melt interface, as well as partially or fully enclosed by the newly crystallized spinel (Fig. 4a). The sulfur-bearing experiment produced chromite showing signs of growth along the margin, as judged by the development of small, euhedral crystal forms projecting from the original chromite surface (Fig. 4b). The amount of Cr_2O_3 in the melt required for chromite saturation at the T–fO_2 conditions of this experiment is estimated to be <0·05 wt % (Roeder & Reynolds, 1991), whereas the Cr_2O_3 content of the Greenland basalt starting material is 0·13 wt %. Consequently, chromite growth is expected, consistent with the textural interpretation. Within the narrow growth zone, a Ru- and S-bearing phase was identified by EDS (Fig. 4c), which is likely to be laurite (RuS_2) as it is the stable Ru-sulfide at the conditions of the experiment.

Chemical characteristics of run-product phases

The composition of spinels produced in experiments shows a distinct shift with respect to their starting material, which is largely due to the imposed oxygen fugacity. Compositional gradients in Figs 5 and 7 are expressed as per cent cation site occupancy to better show the substitutional changes that occur during mineral–melt re-equilibration. At high fO_2 the abundance of Fe^{3+} relative to Fe^{2+} in the melt is elevated, resulting in a considerable gain of Fe_2O_3 in the N-C chromite at the expense of Cr_2O_3 and Al_2O_3 (Fig. 5a). The FeO content of chromites subject to these conditions increases slightly relative to initial values. Time series experiments involving N-C chromite wafers reveal minor gradients in both FeO* and Cr_2O_3 within the glass immediately adjacent to the chromite–glass interface, with FeO* decreasing and Cr_2O_3 increasing (Fig. 6a and b) as the interface is approached. Gradients diminish ~20–30 μm from the interface to concentrations equivalent to the bulk glass. With increased run

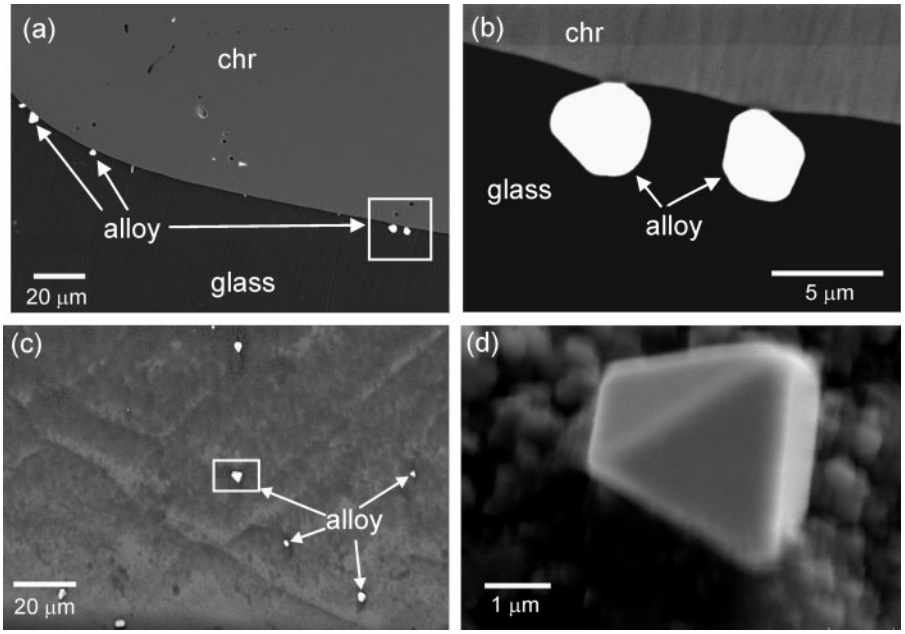

Fig. 2. Scanning electron micrographs of run products (experiment numbers are given in quotes; chr, chromite) from experiments involving re-equilibration between N-C chromite 'slabs' and basalt. (a) Polished section showing Rh–Pt alloy along the interface between chromite slab and melt (experiment 'Rh –2·5 7d', 168 h). (b) Close-up of the region bounded by the white square in (a). Alloy grains show well-developed crystal faces, suggestive of the octahedral form, consistent with the isometric symmetry (hexoctahedral class) of crystalline rhodium. (c) Surface of chromite (experiment 'Rh –2·5 5d') after adhering glass was dissolved in concentrated HF. Light gray corresponds to underlying chromite; darker gray is residual adhering glass. Bright features correspond to Rh–Pt alloys formed at the chromite–melt interface. (d) Close-up of the region bounded by the white square in (c) showing a single, euhedral alloy grain protruding from the chromite surface.

duration, the magnitude of the Cr_2O_3 gradient in the glass appears to decrease. With the exception of a small upturn in concentration at the chromite–melt interface, SiO_2 contents in the glass are uniform (Fig. 6c), as are contents of other major elements not affected by chromite–melt exchange. Experiments that used a 75–90 μm sieved chromite fraction show gradients in Fe_2O_3, Cr_2O_3 and Al_2O_3 in the run-product chromites after 168 h (Fig. 5b). The experiment that used a 35–40 μm sieved fraction run for 336 h is compositionally homogeneous, as well as Fe_2O_3-enriched and Cr_2O_3-, Al_2O_3-depleted relative to the starting material (Fig. 5c). Experiments carried out at intermediate fO_2 (FMQ+1·3) show only slight enrichment of the chromite in Fe_2O_3 in comparison with the initial composition (Fig. 5d). Microprobe traverses from the glass–melt interface across newly formed spinel from cooling experiments (Fig. 7) reveal a decrease in Al_2O_3 and FeO, whereas Cr_2O_3 has increased with respect to the initial R-V spinel composition. The Fe_2O_3 content of the newly formed spinel is essentially the same as that of the starting material. The major element composition of the chromite margins in the S-bearing experiments shows negligible replacement of Cr_2O_3 by Fe_2O_3 and Al_2O_3.

In all experiments, the major element composition of the bulk glass away from any crystal–liquid interface is homogeneous based on multiple point analyses, and similar to the initial Greenland basalt composition. LA-ICP-MS analyses reveal that run product glasses are uniform in their PGE content and generally free of sub-micron-scale alloys. This condition is reached very early in the experiment, as revealed by detailed analysis of experiment Pt/Rh 3h, which was run for 3 h at 1400°C. As shown in Fig. 8a, the time-resolved signal for Pt and Rh in the glass from this experiment is uniform, with the exception of a single, short-duration 'spike', arising from the intersection of a suspended alloy particle in the melt. These isolated 'spikes' are observed in only two of the 11 spots measured across the entire sample. Overall, the run-product glass is also homogeneous, with the variation in concentration between spots similar to counting statistics (Fig. 8b). Longer duration experiments show a similar level of homogeneity and were devoid of 'spikes' in time-resolved spectra. The uniform metal content of run-product glasses is also consistent with the relatively high diffusivity predicted for the PGE in molten silicate. Applying the empirical model of Mungall (2001), we calculate a tracer diffusion coefficient (D) of 1×10^{-6} cm^2/s for divalent cations (the likely valence state of Ir, Pt, Pd, and Rh at the experiment conditions) at 1400°C. Using a diffusion length scale of $\sim(Dt)^{1/2}$ we estimate a transport distance of ~1 mm after 3 h, which is similar to the 1–3 mm radial distance from the centre of the sample to the wire loop. Convection in the sample

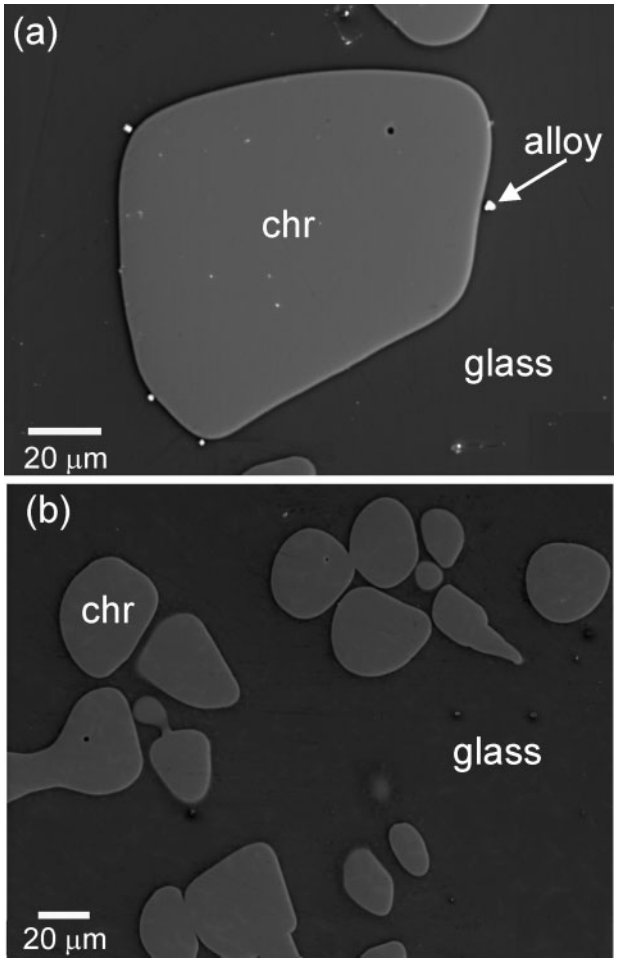

Fig. 3. Scanning electron micrographs of sectioned run products from experiments involving re-equilibration between sieved N-C chromite grains and basalt (experiment numbers and labels as in Fig. 2; sp, spinel). (a) Product of experiment performed using a 75–90 μm sieved chromite fraction showing Pt–Rh alloy along the chromite–melt interface (experiment 'Pt/Rh −2·5b', 168 h). (b) Product of experiment performed using 35–40 μm sieved chromite fraction. The absence of alloys along grain margins should be noted (experiment 'Pt/Rh −2·5', 336 h).

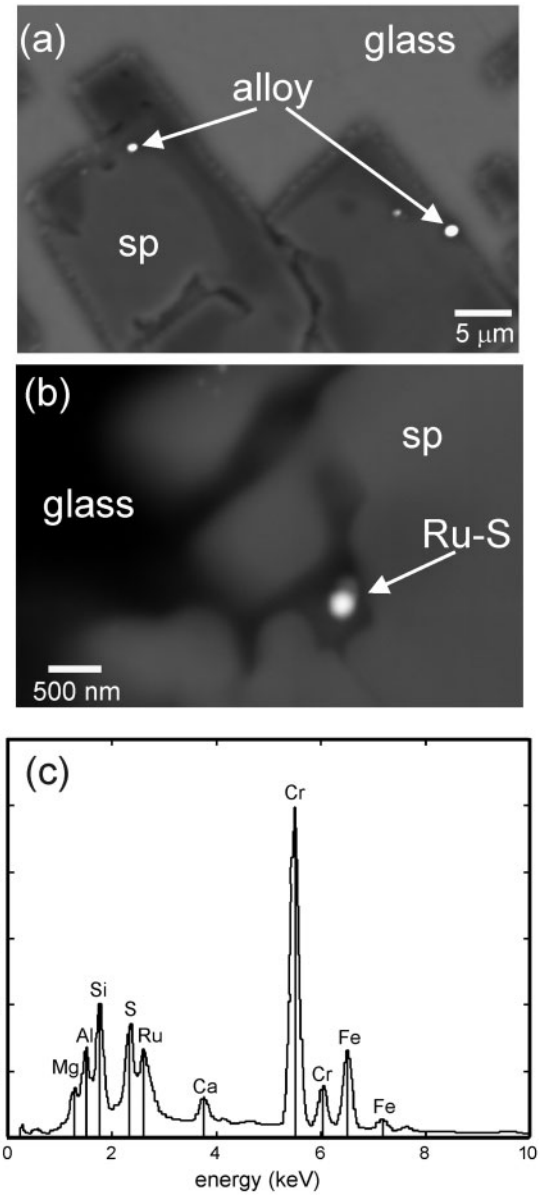

Fig. 4. Scanning electron micrographs and an EDS spectrum from experiments involving growth of chromite on pre-existing seed crystals (experiment numbers and labels as in Fig. 2). (a) Ir–Pt alloys entrapped by crystallizing Cr-spinel during cooling of 30°C over 1 h (experiment 'Ir −7·3 dynamic', 5 h). (b) Ru-sulfide entrapped by crystallizing chromite during cooling of 20°C over 1 h (experiment 'RuS dynamic', 11 h). (c) EDS spectrum of Ru-sulfide grain in (b), showing distinct X-ray peaks at Ru and S, as well as from elements in the surrounding chromite and glass matrix.

would also significantly enhance the homogenization process, although it does not preclude complete melt–metal equilibration (e.g. Borisov, 2001). These results are further corroborated by the experimental work of O'Neill *et al.* (2006), in which basaltic glasses equilibrated at 1400°C and 1 GPa for 2 h were found to have uniform Ru content as far as 3·5 mm from the metal source. Concentrations of the PGE in the glass from some experiments are reported in Table 3, with a comparison with PGE solubilities determined for Fe-free silicate melt (diopside–anorthite eutectic) at the same temperature and fO_2. The agreement between the values determined in this study and those from the published literature is 6–20% for Ru and Pd, but measured solubilities for Pt and Rh are 2–4 times higher than previous determinations. Farges *et al.* (1999) has shown that Pt solubility is higher in silicate melts with a larger proportion of network modifying cations, which scales with the ratio of non-bridging oxygens to tetrahedrally coordinated cations (NBO/T). The value of NBO/T for the diopside–anorthite eutectic composition is ~1, whereas that for the Greenland basalt ranges from 1·2 (ΔFMQ = + 3·8) to 1·5 (ΔFMQ = −1) using Fe speciation calculated from

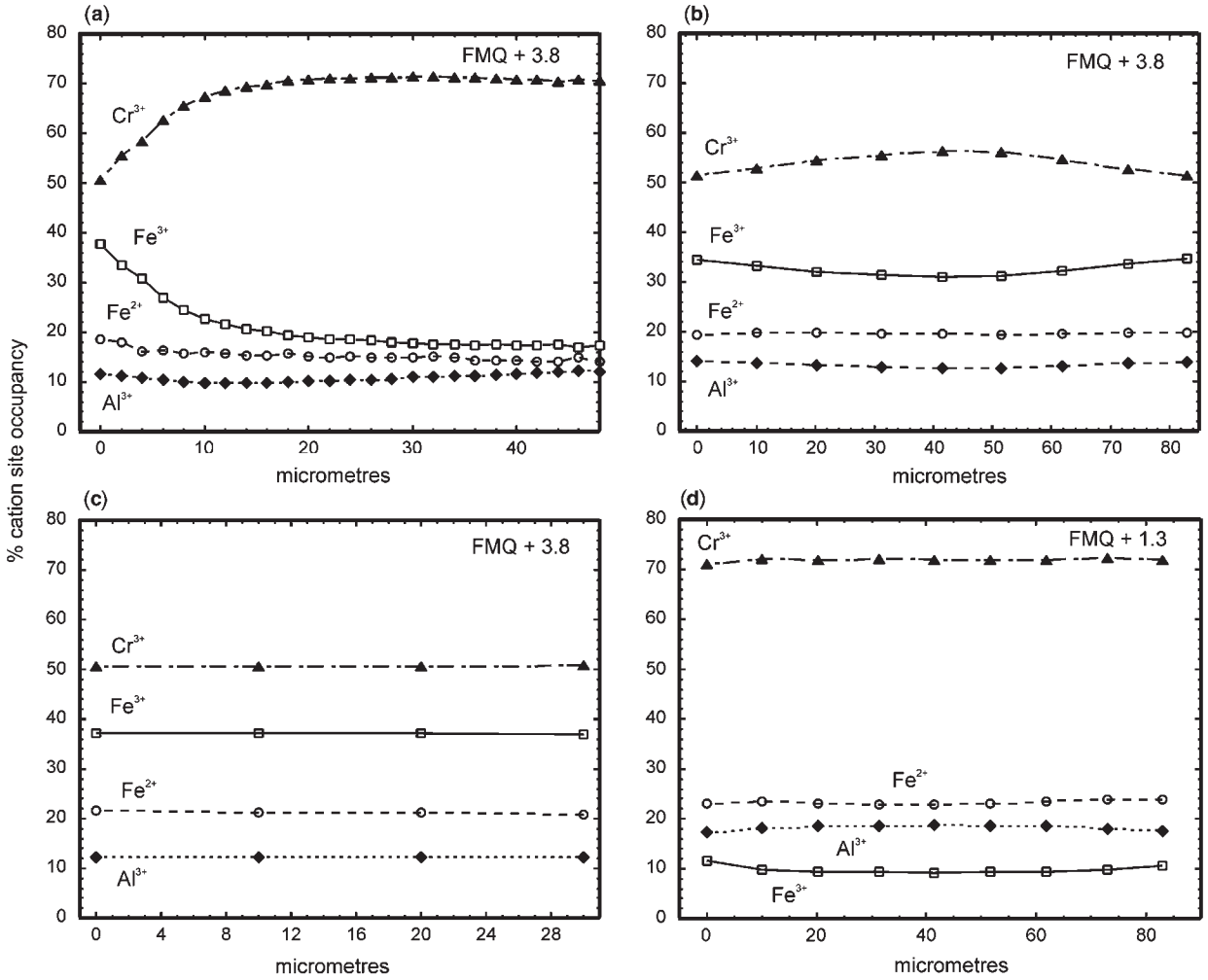

Fig. 5. Electron microprobe traverses in the N-C chromite (crystal–melt interface at $x = 0$) showing the variation in per cent cation site occupancy for (a) chromite slab (experiment 'Rh −2·5 7d', 168 h; sample shown in Fig. 2a and b), (b) 75–90 μm sieved chromite fraction (experiment 'Pt/Rh −2·5b', 168 h; sample shown in Fig. 3a), (c) 30–40 μm sieved fraction (experiment 'Pt/Rh −2·5', 336 h; sample shown in Fig. 3b), (d) 75–90 μm sieved chromite fraction (experiment 'Pt/Rh −5', 168 h). Experiment oxygen fugacities are as indicated.

Kress & Carmichael (1991). It is therefore reasonable that melt composition effects could account for the difference in metal solubilities. The overall homogeneity of the PGE in glasses produced in this study, combined with similarity to levels found in previous solubility determinations, indicates that melts are close to their equilibrium PGE saturation level during spinel growth and re-equilibration.

Metal phases precipitated at the chromite–melt interface generally reflected the composition of the metal mix added (Table 2), and all contain minor Fe. Platinum was also found in alloys, even in those experiments in which the initial metal mix was Pt-free. We suspect the Pt is derived by vapour transport from deposits on the inner wall of the furnace, which accumulate over time by evaporation–deposition from a variety of Pt-bearing components (e.g. unsheathed thermocouple and redox sensor materials, sample capsules, wire loops, etc.).

DISCUSSION

Origin of major element variation within spinel and glass

The spinel and basalt used as starting materials in this study are initially out of equilibrium at the T–fO_2 conditions of our experiments, resulting in chemical potential gradients between these phases. Apart from wholesale dissolution–reprecipitation, equilibrium can be attained only through diffusive exchange between the crystal and melt, the rate and extent of which is dependent on the temperature, the nature of the diffusing species and duration of the experiment. It is certainly possible that some dissolution–repreciptation did occur, but the effects seem to be minor. This process would have deposited on some surfaces a new layer of equilibrium chromite, which would have a uniform composition. Dissolution would serve to remove

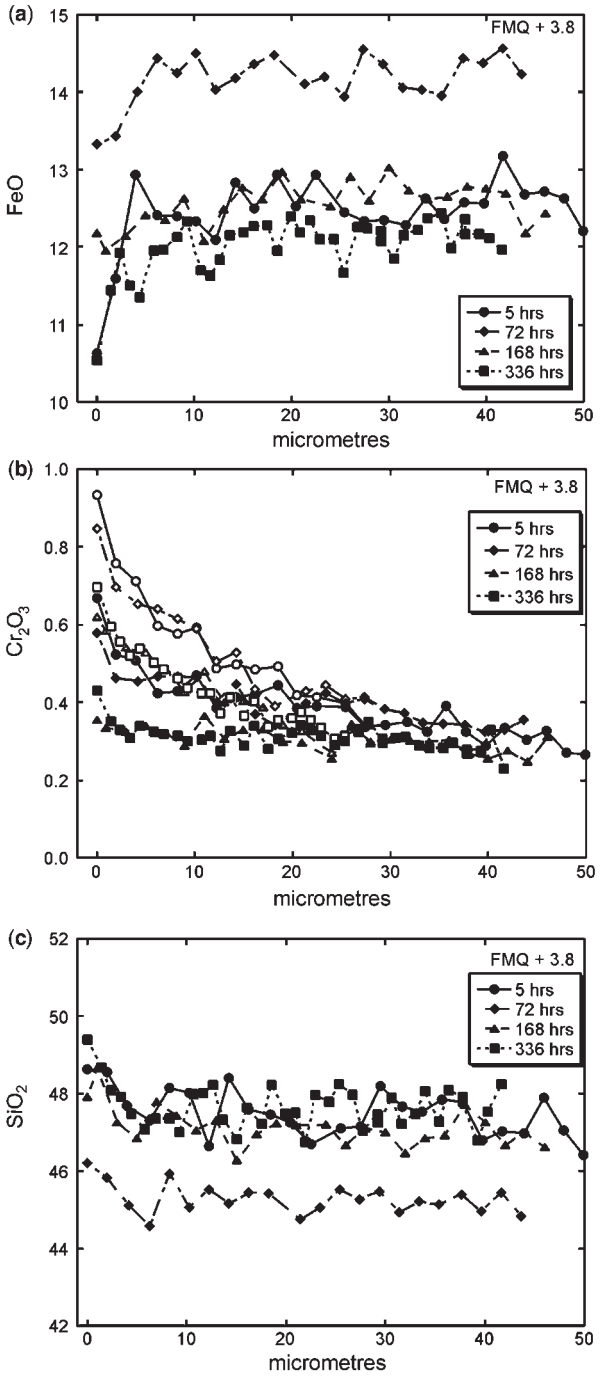

Fig. 6. Electron microprobe traverses in glass adjacent to the chromite–melt interface ($x = 0$) showing the variation in (a) FeO, (b) Cr_2O_3 and (c) SiO_2. Experiments correspond to the 'Rh −2·5' series, which used N-C chromite slabs and were suspended from rhodium loops at log fO_2 of −2·5 for the durations indicated. The raw data for Cr_2O_3 (open symbols) have been corrected (closed symbols) for enhanced Cr X-ray production as a result of proximity to the chromite crystal (see text for details). It should be noted that the somewhat higher FeO and lower SiO_2 in the sample run for 3 days is a mass-balance effect, as it contained a high ratio of melt/chromite, therefore buffering the melt composition against Fe loss to the chromite.

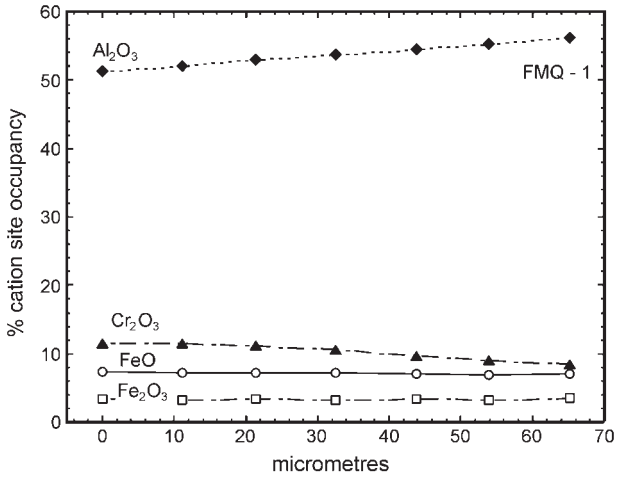

Fig. 7. Electron microprobe traverses in spinel (spinel–melt interface at $x = 0$) showing the variation in cation site occupancy in Cr-spinel produced during cooling 30°C over 1 h (experiment 'Ir −7·3 dynamic'; sample shown in Fig. 2f).

the margins of crystals within which compositional gradients exist, so preservation of gradients will depend on the rate of volume diffusion compared with the rate of dissolution. With the exception of experiment Pr/Rh −2·5, run for 336 h using a small chromite size fraction, all the crystals from experiments preserve well-developed compositional gradients. This suggests that the rate of dissolution is slow compared with volume diffusion, consistent with a low mass flux of Cr, a reflection of low Cr solubility. N-C chromite equilibrated at high fO_2 shows loss of Cr^{3+} and Al^{3+} and gain of Fe^{3+}, resulting in the compositional evolution from chromite to Cr-bearing magnetite. The glass immediately adjacent to these crystals reflects the exchange process, with small local enrichments in Cr_2O_3 and depletions in FeO*. Quench crystallization may also contribute to these gradients. In contrast to the high fO_2 results, cooling experiments carried out at lower fO_2 involving the R-V spinel result in the uptake of Cr^{3+} at the expense of Al^{3+}, with little change in the initial Fe^{3+} content of the spinel. The minimal compositional difference between the N-C chromite and overgrowths produced in the controlled fO_2–fS_2 experiment reflects a small degree of initial chemical disequilibrium between N-C chromite and melt.

Origin of alloy and sulfide at the crystal–liquid interface

The minerals used as starting material contain small amounts of PGE, so it is possible that alloys form in our experiments by mineral dissolution followed by alloy precipitation in the melt phase locally. However, the PGE content of the R-V spinel and N-C chromite is low, so the total mass of alloy that could be formed by this process is very small. For example, a spherical chromite grain with

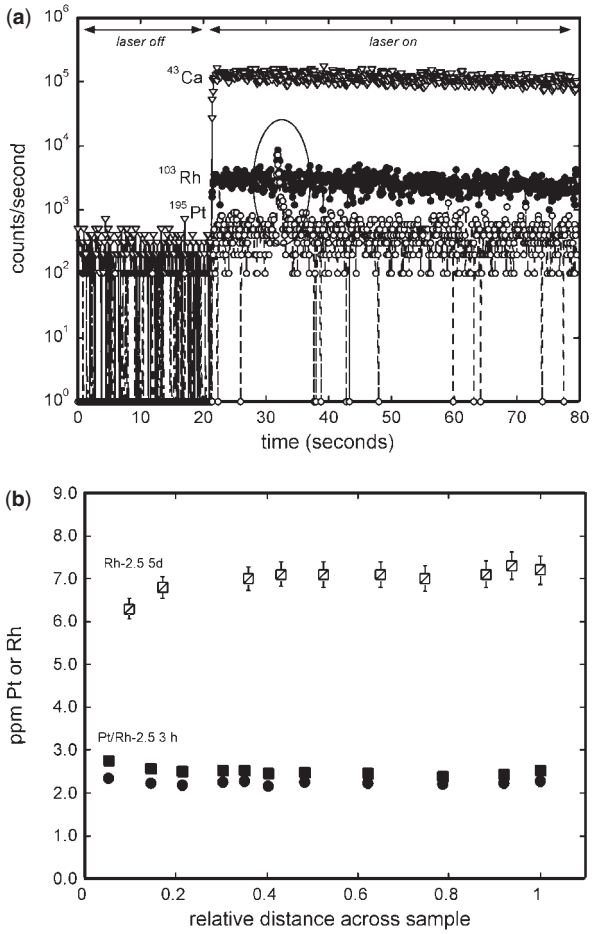

Fig. 8. PGE abundance data for glasses from selected experimental run products. (a) Time-resolved spectrum from a single spot analysis on glass from experiment 'Pt/Rh −2·5 3h' which was run for 3 h at log fO_2 of −2·5. Instrument background was collected for 20 s, followed by laser ablation of the sample. Count rates corresponding to zero have been changed to one for the purposes of plotting on a log scale. The lack of data between zero and 100 counts/s is a consequence of the 10 ms dwell-time chosen for data acquisition, which results in a count rate of 100 counts/s for each ion detected. The circled feature in the spectrum for Rh and Pt is interpreted to be the result of small, undissolved, metal particles intersected during ablation. This spectrum showed the most extreme level of heterogeneity encountered in the 11 spots that were analysed in this sample. (b) Glass concentration of Rh (squares) and Pt (circles) as a function of the relative distance across the run-product (absolute sample diameters range from 3·5 to 6·5 mm).

a radius of 500 μm containing 50 ppb Rh could precipitate a single, spherical, 2 μm diameter crystal if all the Rh in the grain was sequestered to a single nucleation site. Similar estimates apply to the other PGE, indicating that this process cannot account for the abundance of PGE alloy observed. The alloys are also unlikely to have been precipitated from the melt during the quench, as the diffusive transport distance for PGE is too small, and the PGE solubility in the melt phase is too low. Ballhaus *et al* (2006)

Table 3: Comparison of PGE solubility data (ppm)

Experiment number	fO_2	Metal*	Glass	Solubility†	Reference‡
Pd/Ru −2·5b	FMQ+3·8	Ru_{89}	8·9(3·6)	8·4	1
Rh −2·5 5d	FMQ+3·8	Rh_{100}	7·0(0·27)	2·9	2
Rh −2·5 7d	FMQ+3·8	Rh_{100}	10·3(0·3)	2·9	2
Pt/Rh −2·5b	FMQ+3·8	Rh_{30}	4·2(0·1)	2·9	2
Pt/Rh −2·5 3h	FMQ+3·8	Rh_{13}	2·5(0·1)	2·9	2
Rh −5·0	FMQ+1·3	Rh_{100}	0·37(0·03)	0·32	2
Pd/Ru −2·5b	FMQ+3·8	Pd_{87}	51·0(0·8)	64	3
Pd/Ru −5·0	FMQ+1·3	Pd_{87}	12·6(3·0)	14	3
Pt/Rh −2·5 3h	FMQ+3·8	Pt_{87}	2·2(0·1)	0·75	2
Pt/Rh −2·5b	FMQ+3·8	Pt_{70}	1·2(0·1)	0·75	2

*Composition of metal added as alloy or resultant immiscible pairs based on the binary phase diagram. All compositions in wt%.
†Solubility of pure metal in diopside–anorthite eutectic composition at fO_2 of experiment and 1400°C.
‡1, Borisov & Nachtweyh (1998); 2, Ertel *et al*. (1999) with temperature correction of Fortenfant *et al*. (2003); 3, Borisov et al. (1994).

have suggested that PGM may nucleate on pre-existing chromite crystals, as the presence of the chromite surface lowers the surface energy contribution to metal precipitation. This mechanism is not likely to operate in our experiments, as melts are initially PGE undersaturated, and approach saturation by dissolution of the metal wire. Moreover, the presence of very small crystals on the chromite surface is an inherently unstable condition, as these crystals are more soluble than those with a lower surface/volume ratio, which would probably result in dissolution and reprecipitation on the more coarsely crystalline metal wire. There must be a competing gradient in our experiments that allows the alloy crystals to remain at the chromite–melt interface.

Because of the relatively low solubility of PGE in molten silicate at the conditions of our experiments, the formation of alloy grains to the extent observed requires a mechanism involving sustained transport of the metal from a source to the site of deposition at the spinel–melt interface. The metal loop and/or added powder is the most obvious PGE supply, so what is the driving force? Available solubility data suggest that the platinum group metals (M) dissolve in molten silicate as oxide species (MO), according to the general reaction

$$M_{metal} + x/4\ O_2 = MO_{x/2,melt} \quad (1)$$

where x is the valence state of the dissolved metal species. From this relationship it is apparent that lower fO_2 results in decreased metal concentration in the melt at saturation,

which has been confirmed experimentally (Ertel *et al.*, 1999; Borisov & Palme, 2000; Borisov & Walker, 2000). Although the speciation of PGE in sulfur-bearing silicate melts is unknown, a possible reaction for the formation of PGE sulfides takes the form

$$MS_{x/2(sulfide)} + x/4\ O_2 = MO_{x/2(melt)} + x/4\ S2. \quad (2)$$

Like the reaction involving alloy formation, equation (2) indicates that PGE sulfides will be produced as a result of decreased fO_2. From these relations we suggest that PGM formation in our experiments is redox controlled, with gradients in fO_2 developed in response to spinel re-equilibration or growth. This process involves the selective uptake of elements that exist in more than one oxidation state, producing a reduced zone near the solid–melt interface. In the discussion below, we provide a quantitative treatment of these effects as they pertain to our experiments, and to their role in PGM formation in natural magmas.

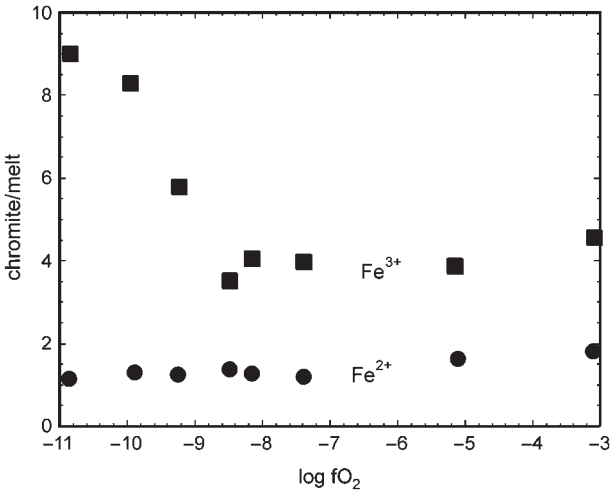

Fig. 9. Chromite/melt partition coefficients for ferric and ferrous iron as a function of oxygen fugacity. It should be noted that at any given fO_2 the partition coefficient for ferric iron exceeds that for ferrous iron. Data from Roeder & Reynolds (1991).

Model of PGM formation during chromite crystal growth

A crystal grows in response to some change in the intensive parameters of its local thermodynamic system. For example, a melt may be perturbed into a state of chromite supersaturation by a change in temperature or by mixing of two magmas along the chromite–olivine cotectic (Irvine, 1977). A chromite grain might nucleate and begin to grow or a pre-existing grain formerly at equilibrium with its host melt may begin to grow anew. Initially, although the system as a whole will not have reached equilibrium, local reversibility may be assumed, and the crystal–melt partitioning will still obey equilibrium thermodynamic constraints at the interface (e.g. Liang, 1999), as also will the partitioning of oxygen between competing polyvalent transition metal oxide components in the silicate melt. Growth of the chromite grain will be accomplished by diffusive transfer of chromite components from a steadily increasing volume of silicate melt, for as long as the melt between widely separated chromite grains remains supersaturated with or out of equilibrium with chromite.

Chromite incorporates Fe^{3+} and Fe^{2+} with a Fe^{3+}/Fe^{2+} ratio always exceeding that of the melt (Fig. 9), and furthermore incorporates Cr^{3+} to the complete exclusion of Cr^{2+} despite the presence of Cr in both valencies in the silicate melt (Roeder & Reynolds, 1991; Berry & O'Neill, 2004). Although previous investigations of Cr speciation in silicate melt have argued for negligible Cr^{2+} in Fe-bearing compositions at moderately oxidizing conditions (e.g. Schreiber & Haskin, 1976), subsequent XANES measurements on samples at high temperature has shown significant amounts of this species (~30% at FMQ; Berry & O'Neill, 2004), which is consistent with chromite solubility measurements (e.g. Roeder & Reynolds, 1991). A compositional boundary layer may be defined as the region between the melt–crystal interface and the outermost extent of the region in which diffusion occurs as a result of chromite growth. This boundary layer will be depleted in both Cr^{3+} and Fe^{3+}. A far-field domain may be defined as the region outside the boundary layer where diffusion has not yet affected the composition of the melt.

The homogeneous reaction within the silicate melt

$$Fe^{3+} + Cr^{2+} = Fe^{2+} + Cr^{3+} \quad (3)$$

may be assumed to take place instantaneously, such that the fO_2 defined by each of the chromic/chromous and ferric/ferrous ratios will be identical. Because of the net loss of the oxidized species Fe^{3+} and Cr^{3+} from the melt into the growing crystal, the melt as a whole will be somewhat reduced throughout the compositional boundary layer, increasingly so toward the melt–crystal interface. When equilibrium is attained in the bulk magma, the small perturbation in the fO_2 imposed by the growth of additional chromite will have been felt throughout the magma; however, at any given time during the approach to equilibrium, the lowest fO_2 experienced within the system will always be at the chromite–melt interface.

We believe that this effect is simulated by our experiments in which chromite growth is driven by a decrease in temperature, and alloys form by the ensuing gradient in fO_2. To model this process quantitatively, we have employed simple empirical relations published by Roeder & Reynolds (1991) for chromic/chromous and ferric/ferrous ratios as functions of fO_2, combined with a least-squares fit to their data for chromite solubility in the melt composition

Table 4: Compositional data to determine effect of chromite crystallization on local fO_2

Oxide	Initial 401 diabase*	Chromite removed	Melt in contact with chromite*
SiO_2	49·02		49·02
TiO_2	1·87	1·82	1·86
Al_2O_3	15·25	21·64	15·06
Fe_2O_3	1·84	11·74	1·74
FeO	11·22	15·29	11·08
MnO	0·19		0·19
MgO	5·99	17·92	5·83
CaO	8·51		8·51
Na_2O	2·93		2·93
K_2O	1·06		1·06
P_2O_5	0·19		0·19
Cr_2O_3	0·13	31·59	0·093
CrO	0·042		0·03
$X_{FeO1·5}/X_{FeO}$	0·148		0·145
log fO_2†	−7		−7·025
$X_{CrO1·5}/X_{CrO}$	2·82		2·77
log fO_2‡	−7		−7·025

Compositions are in wt%.
*Cr_2O_3 solubility (wt%) = 0·0005(log fO_2)^4 + 0·0114(log fO_2)^3 + 0·0985(log fO_2)^2 + 0·3541(log fO_2) + 0·4879.
†Calculated using the variation in molar $X_{FeO1·5}/X_{FeO}$ with fO_2 for 401 diabase (Roeder & Reynolds, 1991).
‡Calculated using the variation in molar $X_{CrO1·5}/X_{CrO}$ with fO_2 for 401 diabase (Roeder & Reynolds, 1991).

they referred to as '401 diabase' (see the third footnote to Table 4). We considered these parameters as functions of fO_2 at 1300°C to estimate the composition of the melt in the interface surrounding a chromite crystal growing from a melt initially containing 1800 ppm Cr_2O_3 at 1300°C with an ambient intrinsic log fO_2 of −7 (∼FMQ). The model parameters and results are presented in Table 4. Under the chosen conditions the equilibrium solubility of Cr_2O_3 is only 1260 ppm, so chromite is precipitated. We estimate the composition of the chromite using the MELTS program (Ghiorso & Sack, 1995), which is calibrated for this phase using the experimental work of Murck & Campbell (1986) and Roeder & Reynolds (1991). An appropriate quantity of this chromite is subtracted from the melt composition to bring the concentration of Cr_2O_3 in the residual melt to 1260 ppm, and the concentrations of Mg, Al, Fe^{3+}, Fe^{2+}, and Cr^{3+} are adjusted accordingly. The resulting nominal composition is strongly depleted in Cr^{3+} relative to Cr^{2+}, with the result that the fO_2 calculated from Cr^{3+}/Cr^{2+} in the residual melt is not in agreement with that calculated from Fe^{3+}/Fe^{2+}. To maintain local reversible equilibrium, exchange of oxygen via reaction (3) must proceed until both ratios record the same fO_2 in the melt; in our model we accomplish this iteratively by adjusting the relative proportion of Fe^{3+} and Cr^{3+} while maintaining an overall oxygen mass balance. When this process is completed, both Cr^{3+}/Cr^{2+} and Fe^{3+}/Fe^{2+} ratios indicate that the fO_2 has fallen below log fO_2 of −7, forcing a re-evaluation of the solubility of Cr_2O_3* (i.e. total Cr oxide in the melt expressed as Cr_2O_3) in the melt and a repeat of the calculation of chromite removal. This iterative process is continued until the amount of chromite removed in the model leaves a Cr_2O_3* concentration in the melt that is at equilibrium at the fO_2 determined by matching Cr^{3+}/Cr^{2+} and Fe^{3+}/Fe^{2+} ratios after chromite removal. The final calculated melt composition corresponds to that expected to form in the boundary layer around the growing chromite crystal at the beginning of a transient episode of chromite growth from a melt supersaturated with respect to chromite. The boundary layer is slightly but significantly depleted in Fe^{3+} and Cr^{3+} relative to the far-field composition, with an equilibrium Cr_2O_3* content of 1270 ppm and an intrinsic log fO_2 of −7·0254.

Borisov & Palme (2000) provided a comprehensive summary of existing highly siderophile elements (HSE) solubility data, including an assessment of the effects of T, fO_2 and melt FeO content. They showed that mantle-derived magmas crystallizing at or below the FMQ buffer have PGE contents sufficient to be saturated in Pt-, Ru- and Ir-bearing alloy. More recent estimates of the solubility of osmium in molten silicate are somewhat variable; whereas Brenan *et al.* (2005) measured values of ≤10 ppb at 1350°C and FMQ + 0·6 for an Fe-bearing basalt, solubilities determined by Fortenfant *et al.* (2006) for the anorthite–diopside eutectic composition at similar conditions are about 100 times higher. In any case, it seems likely that once saturation in Ru-bearing alloy is achieved, Os will be strongly partitioned into this phase, as there is complete solid solution in the Os–Ru system at magmatic temperatures (Tylkina *et al.*, 1962). The effect of sulfur on these solubility relations is unknown, nor have the solubilities of PGE-sulfides in molten silicate been determined, so it is difficult to assess whether sulfur-bearing mafic suites are close to alloy or laurite saturation. It seems likely, however, that sulfur-poor magmas from which chromite precipitates are probably close to alloy saturation so that even small changes in redox state can cause micronuggets of alloy to form throughout the compositional boundary layer. The magnitude of this solubility change will depend on the oxidation state of the dissolved PGE oxide species. PGE solubility measurements suggest that at the fO_2 relevant to the genesis of terrestrial basalts (FMQ ± 1 or so), Pd is dominantly in the univalent state (Borisov *et al.*, 1994), Ir, Rh, Pt are divalent (Borisov & Palme, 1995, 1997; O'Neill *et al.*, 1995; Ertel *et al.*, 1999), and Ru and Os are trivalent (Borisov &

Nachtweyh, 1998; Borisov & Walker, 2000; Fortenfant *et al.*, 2006). In the example above, the reduction of fO_2 by 0·0254 log units will diminish Os and Ru solubility each by 4%. Solubilities of the divalent PGE will be reduced by about 3%. The formation of micronuggets would be promoted most strongly in the immediate interfacial region because this is where the fO_2 is reduced the most. Micronuggets with sizes in the nanometer to micrometer range will have negligible Stoke's settling velocities, with the result that they will not be advected away from the growing crystal face by their own negative buoyancy. Whereas melt components rejected by the growing crystal (including PGE not present in micronuggets) can diffuse away from the interfacial region with diffusivities in mafic liquids of the order of 10^{-6} cm^2/s (e.g. Mungall, 2001), the removal of nanometer-scale micronuggets from the interfacial region by Brownian motion will be impeded by their relatively large size. The Stokes–Einstein relation predicts a diffusivity via Brownian motion for micronuggets of some two orders of magnitude less than the network-former diffusivity in a given melt if the particles in question are about two orders of magnitude larger than the network-forming tetrahedra. Larger particles will be even more sluggish, with the result that alloy micronuggets, once formed, will tend to be overgrown by the advancing crystal–melt interface, thus becoming inclusions in the growing chromite crystal.

According to the classic Gibb's treatment of crystal nucleation kinetics, if a melt contains an amount of a component exactly equal to its equilibrium solubility, nucleation of crystals of that component will be impeded by an energy barrier resulting from the contribution of surface energy to the total internal energy of very small crystal nuclei. Formation of stable crystal nuclei therefore requires a small perturbation of the state of the system to supersaturation with respect to the solid phase; once a crystal nucleus has attained the critical size required for thermodynamic stability it will continue to grow from the mildly supersaturated medium until the melt returns to a stable equilibrium. Henceforth, gradual reductions in the solubility of the solid phase will lead to continued growth of those solid phases that have already nucleated and no new crystals are expected to form in the far-field region. As a result, nucleation and growth of alloy crystals could be expected to be restricted to those portions of the magma that are supersaturated with respect to alloy; the far-field volume between chromite crystals should thus remain free of alloy particles while these particles continue to grow at their initial nucleation sites on the margins of chromite grains. The consequence of this barrier to nucleation of alloy anywhere outside the slightly reduced compositional boundary layer of the chromite crystals is that the entire excess PGE budget of the chromite-supersaturated melt will be forced to travel to the nucleation sites of the alloy grains on the margins of the chromite crystals. In this way the growing chromite crystals act as collectors and sweep all of the excess PGE into small alloy nuggets at their margins. The diffusivity of the PGE components in the silicate melt should be within an order of magnitude of the diffusivities of the major element components whose transfer permits chromite crystal growth (e.g. Mungall, 2001), with the result that the timescale of PGE transfer to the boundary layer is similar to that of crystal growth. In other words, there is no kinetic barrier to the efficient collection of the entire excess PGE budget in the chromite-supersaturated melt into alloy particles within the compositional boundary layer surrounding the growing chromite crystal.

In the model described above, the alloy-saturated melt initially contained 5·98 ppb Ru (Borisov & Nachtweyh, 1998); after chromite growth ceased the newly equibrated melt would contain 5·74 ppb Ru. All of the 0·24 ppb Ru lost to the melt would now reside in alloy grains on the margins or included within the newly added growth zone mantling the chromite crystals. The mass of chromite produced in this growth event corresponds to 0·17% of the mass of the whole system but will now contain 4% of the Ru formerly dissolved in the melt; the concentration of Ru in the bulk mixture of chromite and alloy grains, excluding any Ru actually dissolved in solid solution within the chromite grain, is therefore $4/0{\cdot}17 = 24$ times higher than that initially present in the melt. In other words, the predicted effects of boundary layer crystallization of alloy nuggets would cause chromite and alloy to crystallize together with an effective mineral–melt partition coefficient of 24 even if the actual equilibrium chromite/melt partition coefficient was zero. The resulting chromite crystal would contain 138 ppb Ru in the form of miniscule alloy inclusions within a chromite crystal that itself may contain absolutely no dissolved Ru.

Model for alloy nucleation during re-equilibration of spinels

In some instances a spinel crystal will find itself surrounded by silicate melt with which it is not in equilibrium, either during magma mixing or as a result of settling through a stratified magma column. This situation was deliberately induced in most of our experiments, and it is expected to occur in natural systems fairly often. For example, Mondal & Mathez (2007) have suggested that the UG2 chromitite (Bushveld Complex) was formed by injection of new batches of magma with a suspended load of chromite crystals. It is entirely possible that, because of the low solubility of Cr in molten silicate, the chromite crystal will neither grow nor dissolve to a significant extent, but will simply exchange cations with the surrounding silicate melt. If the existing crystal has Cr^{3+}/Cr^{2+} or Fe^{3+}/Fe^{2+} ratios lower than those that would be at equilibrium with the surrounding melt, then the ensuing reaction will draw Cr^{3+} or Fe^{3+}, or both, from the melt,

replacing them with Al^{3+} or other trivalent cations. This process is accomplished by exchanges such as

$$Fe^{2+}Al_2^{3+}O_{4(spinel)} + 2(Fe^{3+},Cr^{3+})_{(melt)} = Fe^{2+}(Fe^{3+},Cr^{3+})_2O_{4(spinel)} + 2Al^{3+}_{(melt)} \quad (4)$$

and

$$Ti^{4+}Fe^{2+}{}_2O_{4(spinel)} + 2(Fe^{3+},Cr^{3+})_{(melt)} = Fe^{2+}(Fe^{3+},Cr^{3+})_2O_{4(spinel)} + Ti^{4+}_{(melt)} + Fe^{2+}_{(melt)} \quad (5)$$

both of which result in a transfer of ferric or chromic ions from the silicate melt into the chromite crystal. Similar exchanges might occur if chromite crystallized from a mafic melt falls into a more magnesian melt having relatively high Cr/Al, such as the composition of the primitive magma of the Bushveld complex (Harmer & Sharpe, 1985). A similar scenario might occur if the 'A-type' and 'U-type' magmas proposed by Irvine *et al.* (1983) were to mix. Although the eventual state of the system at equilibrium would consist of a chromite crystal with a composition in equilibrium with the mafic liquid, it will first pass through a transient state in which the melt composition at the boundary of the crystal is in local equilibrium with the crystal. In this exchange process there may not be any net change in size of the chromite crystal but, nevertheless, the perturbation in fO_2 described above for the case of chromite supersaturation will still obtain. While the chromite grain remains out of equilibrium with its host melt, the rate of mass exchange between crystal and melt will be dominated by solid-state diffusion within the crystal, which is expected to be much slower than diffusion in the silicate melt. The reduction in fO_2 within the diffusive boundary layer around the chromite crystal might therefore be expected to persist for a considerable length of time.

To model this process, we consider the exchange that occurred when we placed the N-C spinel crystals into the Greenland basalt in experiment Pt/Rh −5, carried out at log $fO_2 = -5$ (FMQ+1·3). We selected this experiment because the dominant exchange reaction is of the type in equation (4), and involves Fe^{3+} only, as the gradients in Cr^{3+} within the crystal are negligible (Fig. 5d). Experiments performed at higher fO_2 show significant exchange of Cr^{3+} from the crystal to the melt, although the uptake of Fe^{3+} exceeds the loss of Cr^{3+}, on a molar basis, because of the additional loss of Al^{3+}. Those experiments are more difficult to model, however, as the speciation of Cr and Fe would have to calculated iteratively along the diffusion profile. In contrast, for the exchange of species involving a single element, there is an analytical solution to the diffusion problem, as described below.

The situation at the boundary of a spinel crystal immersed in melt with which it is not at equilibrium corresponds closely to the chemical diffusion problem referred to by Crank (1975) as the infinite composite medium. A modification of Crank's (1975) solution to this problem was presented by Malkovich (2000) to accommodate the case in which solute concentration is initially non-zero in both phases:

$$C_i^{liq} = \frac{1}{\sigma+1}\left[\left(\frac{C_i^{sp^*}}{k} + \sigma C_i^{liq^*}\right) + \left(\frac{C_i^{sp^*}}{k} - C_i^{liq^*}\right) \times \mathrm{erf}\left(\frac{x}{\sqrt{4D_i^{liq}t}}\right)\right] \quad (6)$$

$$C_i^{sp} = \frac{1}{\sigma+1}\left[\left(C_i^{sp^*} + k\sigma C_i^{liq^*}\right) + \sigma\left(C_i^{sp^*} - kC_i^{liq^*}\right) \times \mathrm{erf}\left(\frac{x}{\sqrt{4D_i^{sp}t}}\right)\right] \quad (7)$$

where D_i^{sp} and D_i^{liq} are the diffusivity of species i in spinel and liquid, C_i^{sp*} and C_i^{liq*} are the initial concentration of species i in both phases (each is assumed to be homogeneous initially), C_i^{liq} and C_i^{sp} are the concentrations of species i at time t and distance x from the interface ($x>0$ within chromite, $x<0$ within liquid), k is the partition coefficient expressing the ratio of the concentration of species i in liquid to spinel at equilibrium, and σ is defined as

$$\sigma = \frac{1}{k}\left(\frac{D_i^{liq}}{D_i^{sp}}\right)^{1/2}. \quad (8)$$

In this example, equations of this type can be written for each interdiffusing Fe species (Fe^{3+}, Fe^{2+}). Inspection of equations (6) and (7) shows that the interfacial compositions of both spinel and liquid, given by the first terms on the right-hand sides, are attained instantaneously at $t=0$, and do not change thereafter as long as the diffusion profiles do not encounter the limit of either phase (i.e. both phases remain effectively semi-infinite). It is therefore not necessary to evaluate the entire diffusion profile to estimate the change in solubility of PGE at the interface during diffusive re-equilibration of chromite and melt.

To implement equations (6) and (7) we require estimates of the partition and diffusion coefficients for Fe^{2+} and Fe^{3+} in both chromite and liquid. We assume that the composition of the margin of the spinel in the Pt/Rh −5 experiment represents the composition in equilibrium with the Greenland basalt at the T–fO_2 conditions of the experiment. The speciation of ferric and ferrous iron in the silicate melt is calculated using the calibration of Kress & Carmichael (1991). Comparison of the compositions of melt and chromite yields the requisite partitioning information (Table 5). These partition coefficients are assumed to be approximately constant over small ranges in composition. We note that the assumption of instantaneous

Table 5: Compositional data to determine effect of N-C spinel re-equilibration with Greenland basalt on interface fO_2

	Greenland basalt		Pt/Rh −5 spinel			N-C spinel		Greenland basalt	
	wt%	mol%	wt%	mol%	k^*	wt%	mol%	interface wt%†	interface mol%
SiO_2	44·58	41·62	—	—	—	—	—	44·58	45·19
TiO_2	4·55	3·20	0·92	0·72	0·23	0·13	0·16	4·55	3·47
Al_2O_3‡	6·97	7·67	9·26	11·39	1·49	10·68	20·95	6·97	4·16
Fe_2O_3	3·73	2·62	10·58	8·31	3·17	5·48	6·86	3·55	1·35
FeO	10·98	8·57	8·13	7·10	0·83	9·90	13·78	11·00	9·33
MnO	0·164	0·13	0·17	0·15	1·17	0·16	0·23	0·16	0·14
MgO	15·12	21·05	16·69	25·98	1·23	15·44	38·31	15·12	22·85
CaO	10·24	10·24	—	—	—	—	—	10·24	11·12
Na_2O	1·64	2·97	—	—	—	—	—	1·64	1·61
K_2O	1·21	1·44	—	—	—	—	—	1·21	0·78
P_2O_5	0·55	0·43	—	—	—	—	—	0·55	0·43
Cr_2O_3	0·0658	0·049	56·15	46·34	954	58·63	77·15	not modeled	not modeled
$X_{FeO1·5}/X_{FeO}$		0·306							0·290
log fO_2§		−5·00							−5·12

*Molar spinel/melt partition coefficient, calculated from composition of Pt/Rh −5 spinel and Greenland basalt.
†Composition at the spinel–melt interface after diffusive exchange for 7 days at 1400°C calculated using equations (6) and (7) (see text for more details).
‡Mol% is calculated on a single cation basis (i.e. $AlO_{1·5}$, $FeO_{1·5}$) to simplify mass balance.
§Log fO_2 calculated from molar $X_{FeO1·5}/X_{FeO}$ using the calibration of Kress & Carmichael (1991).

homogeneous equilibration of Fe^{2+}/Fe^{3+} in the melt necessitates the adoption of a single bulk diffusion coefficient for Fe in the melt, with values intermediate between the diffusivities of the elements in their two different oxidation states. Choi (2004) measured multicomponent diffusion coefficients in the nominally nine-component system SiO_2–TiO_2–Al_2O_3–FeO–MgO–CaO–Na_2O–K_2O–P_2O_5 at 1400°C and 1 GPa. In those experiments, samples were first equilibrated in air at 1400°C, so the measured diffusivity for FeO is actually that of FeO and Fe_2O_3 combined, as in the example considered here. Choi's (2004) measured eigenvalue for FeO diffusion, considering SiO_2 as the solvent, is 8×10^{-7} cm^2/s^2 and for the composition employed in our experiments we calculate a single bulk diffusion coefficient for Fe in the melt of 1×10^{-6} cm^2/s.

In principle, estimates of the relevant diffusion coefficients in spinel could be made from the concentration gradients produced in the experiments performed in this study. However, the gradients in Fe^{2+} in run-product chromites are small, as the chromite/melt partitioning for Fe^{2+} is near unity (Fig. 9). For the case of Fe^{3+}, concentration profiles do not conform to simple error functions, which is a consequence of the time evolution of the interface composition (because of mass-balance effects) and probably non-linear activity–composition relations along the concentration profile. Instead, we have obtained estimates of these values from previous diffusion studies. The diffusivities of Cr^{3+} and Co^{2+} in $CoCr_2O_4$ spinel over the temperature range of interest are

$$D^{sp}_{Cr} = 2\exp\left(\frac{-293\ \text{kJ/mol}}{RT}\right) \quad (9)$$

and

$$D^{sp}_{Co} = 10^{-3}\exp\left(\frac{-213{\cdot}5\ \text{kJ/mol}}{RT}\right) \quad (10)$$

(Sun, 1958). To a first approximation, we anticipate that the diffusivities of trivalent cations will be subequal and different from those of divalent cations in a given spinel. We therefore use equation (9) to calculate the diffusivity of Fe^{3+} in the spinel at 1400°C, which yields a value of $1{\cdot}4 \times 10^{-9}$ cm^2/s. At the same temperature, Sun (1958) estimated the diffusivity of divalent cations to be $2{\cdot}2 \times 10^{-10}$ cm^2/s; however, Liermann & Ganguly (2002) found that the diffusivities of Mg^{2+} and Fe^{2+} in aluminous spinels were identical within experimental error and gave the relation

$$D^{sp}_{Fe} = 1{\cdot}8 \times 10^{-5}\exp\left(\frac{198\ \text{kJ/mol}}{RT}\right) \quad (11)$$

allowing the calculation of the diffusivity of divalent cations in our case to be $1{\cdot}2 \times 10^{-11}$ cm^2/s, significantly less

than Sun's (1958) measurement. Lacking a better constraint, we choose a value intermediate between these two estimates and propose a diffusivity of Fe^{2+} in spinel at 1400°C of $1{\cdot}2 \times 10^{-10}$ cm^2/s. The much higher diffusivity of trivalent relative to divalent species in spinel was attributed by Sun (1958) to the relative proximity of holes in the crystal lattice through which the cations diffuse.

The calculated gradient in Fe^{3+}/Fe^{2+} in melt and chromite after 7 days at FMQ + 1·3 and 1400°C is shown in Fig. 10. Because of the high diffusivites in the melt, calculated gradients in this phase are small, and most pronounced in a narrow zone near the crystal–liquid interface. Whereas the log fO_2 has been imposed at −5·0 in the far field, yielding molar $X_{FeO1.5}/X_{FeO}$ in the melt of 0·306, the diffusion model predicts $X_{FeO1.5}/X_{FeO}$ of 0·290 in the compositional boundary layer, corresponding to log fO_2 of −5·12. This decrease in fO_2 of 0·12 log units would cause a drop in the solubility of Pt and Rh of ∼15%, and reduction in the solubility of both Ru and Os of ∼22%. This is a significant change in metal solubility that would be expected to cause instantaneous precipitation of alloy grains on the margin of the chromite crystal even though the host magma might even be undersaturated with respect to the PGE. For the same reasons as given in the previous discussion of chromite crystal growth, the drop in alloy solubility would thus lead to a drop in the chemical activity of the PGE in the diffusive boundary layer and would therefore promote a continuous flux of PGE towards the growing alloy particles for as long as the chromite crystal remained out of equilibrium with the silicate melt in the far field.

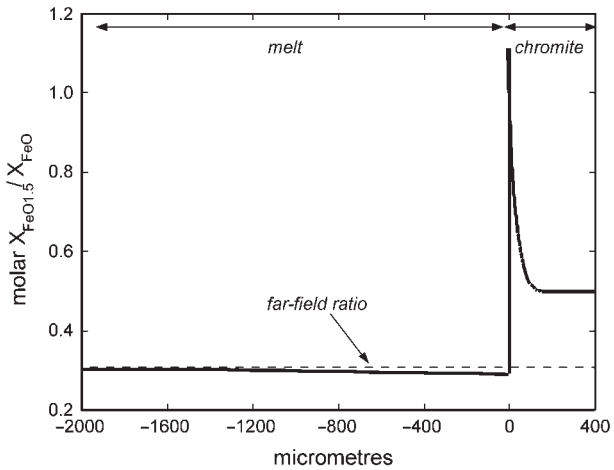

Fig. 10. Modeled effect of chromite–liquid re-equilibration on redox gradients near the crystal–liquid interface. The model involves immersion of un-equilibrated N-C spinel in Greenland basalt at 1400°C and FMQ + 1·3 for 7 days (similar to experiment Pt/Rh −5; Table 2). The variation in the molar ratio of Fe^{3+}/Fe^{2+} (expressed as $X_{FeO1.5}/X_{FeO}$) as a function of position in melt and chromite is calculated using equations (6) and (7), assuming the parameters specified in the text. The decrease in Fe^{3+}/Fe^{2+} in the melt as the chromite–melt interface is approached should be noted; this is a consequence of the selective uptake of Fe^{3+} relative to Fe^{2+} in the chromite structure. The 'far-field' value of $X_{FeO1.5}/X_{FeO}$ corresponds to △FMQ+1·3, whereas the value at the chromite–melt interface is equivalent to △FMQ + 1·18.

The drop in PGE alloy solubility in the compositional boundary layer would persist for as long as it took the diffusion profile within the spinel xenocryst to reach the centre of the crystal. Once the diffusion profile began to relax, the composition of the boundary layer would gradually return to that of the far-field concentration, provided that the melt composition was effectively buffered by an infinite reservoir of the far-field melt. If the crystal shrank or did not change in size, then the alloy grains at the interface would eventually redissolve in the ambient melt, after the crystal had reached equilibrium with the surrounding far-field melt. This prediction is confirmed by the results of the experiments involving the sieved chromite grains, in which the longest duration experiment involving the smallest size fraction yielded homogeneous grains, and alloy-free margins (Figs 2d and 3c). In this case, however, the far-field melt is not PGE undersaturated, but the crystals dissolve and reprecipitate on the coarsely crystalline PGE wire in response to the 'normal' solubility gradient driven by variation in surface curvature. We note that if the re-equilibration process in natural systems involved even a small amount of additional chromite crystal growth, then the alloy grains formed in the transient diffusive re-equilibration event would be trapped within the chromite crystal and henceforth would remain unable to re-equilibrate or redissolve in the ambient melt.

In summary, either if magma mixing causes the precipitation of new chromite grains from a silicate magma that is at or near PGE alloy saturation, or if mixing or similar processes permit the transfer of chromite of basaltic origin into a more magnesian magma, the resulting transient episode of chromite–melt equilibration can be expected to cause the precipitation of alloy particles around the chromite crystal margin. Growth of the chromite grain will trap these particles and lead to effective bulk chromite/melt partition coefficients that are much higher than true equilibrium partitioning would dictate. After the chromite crystal has reached equilibrium with the melt, it will have the same composition as all other chromite crystals in the magma, but the presence of trapped grains of platinum-group minerals will preserve a record of its history as a xenocryst whose composition was initially far from equilibrium with the magma.

Different spinel crystals may have had different histories. A small number of originally Al-rich spinel xenocrysts may undergo the processes described here, acquiring large numbers of PGM inclusions, after which they will gradually equilibrate with the host magma until their bulk

compositions are identical to those of other spinel crystals that grew directly from the host melt. This phenomenon could account for the common observation of wildly differing inclusion populations in different chromite crystals.

CONCLUSIONS

The experiments performed in this study show that PGM alloys will precipitate along the margins of chromite crystals that are out of equilibrium with a melt phase or during chromite growth. We propose that the mechanism by which this occurs involves a redox gradient produced by local reduction within the chromite–melt interfacial region as a consequence of the selective uptake of trivalent Cr and Fe relative to the divalent species. We present models of chromite growth and diffusive re-equilibration in which the magnitude of the fO_2 reduction is estimated by assuming local equilibrium, with crystal and melt compositions determined from this study, or calculated using the experimental results of Roeder & Reynolds (1991) and the MELTS thermodynamic program (Ghiorso & Sack, 1995). Model results indicate that metal solubilities will decrease by several per cent during transient growth, and by as much as 20% during re-equilibration events, providing a potent driving force for alloy formation and sequestration in magmatic chromite crystals. We conclude that chromite crystallization or re-equilibration with a melt could explain the chromite–PGM association in natural magmatic systems that are close to PGE saturation. Our work indicates that the well-known observation of chromite as a 'collector' for PGM is to be expected in light of its known magmatic behaviour.

ACKNOWLEDGEMENTS

We are grateful for the reviews by C. Ballhaus, A. Borisov and E. Mathez, and the editorial comments of R. Frost, which have improved the quality of presentation. We also wish to acknowledge the large number of anonymous researchers who provided helpful commentary on the less-developed iterations of this work. Funding for this research was provided through a GSA Research Grant to C.S.F. and NSERC Discovery and Equipment grants to J.M.B. and J.E.M. We greatly appreciate the efforts of Richard Ash in the UMD Plasma Lab. A portion of this study was funded by NSF grants 0337621 and 0739006 to W.F.M.

REFERENCES

Andrews, D. R. A. & Brenan, J. M. (2002). Phase-equilibrium constraints on the magmatic origin of laurite + Ru–Os–Ir alloy. *Canadian Mineralogist* **40**, 1705–1716.

Ballhaus, C. & Sylvester, P. (2000). Noble metal enrichment processes in the Merensky Reef, Bushveld Complex. *Journal of Petrology* **41**, 545–561.

Ballhaus, C., Bockrath, C, Wohlgemuth-Ueberwasser, C., Laurenz, V. & Berndt, J. (2006). Fractionation of the noble metals by physical processes. *Contributions to Mineralogy and Petrology* **152**, 667–684.

Barin, I. (1995). *Thermochemical Data of Pure Substances*. New Yprk: VCH.

Barnes, S. J. & Roeder, P. L. (2001). The range of spinel compositions in terrestrial mafic and ultramafic rocks. *Journal of Petrology* **42**, 2279–2302.

Barnes, S.-J., Naldrett, A. J. & Gorton, M. P. (1985). The origin of the fractionation of platinum- group elements in terrestrial magmas. *Chemical Geology* **53**, 303–323.

Berry, A. J. & O'Neill, H. S. C. (2004). A XANES determination of the oxidation state of chromium in silicate glasses. *American Mineralogist* **89**, 790–798.

Bockrath, C., Ballhaus, C. & Holzheid, A. (2004). Stabilities of laurite RuS_2 and monosulfide liquid solution at magmatic temperature. *Chemical Geology* **208**, 265–271.

Borisov, A. (2001). Loop technique: dynamics of metal/melt equilibration. *Mineralogy and Petrology* **71**, 87–94.

Borisov, A. & Nachtweyh, K. (1998). Ru solubility in silicate melts: experimental results in oxidizing region. *Lunar and Planetary Science* **XXIX**, Abstract 1320.

Borisov, A. & Palme, H. (1995). The solubility of iridium in silicate melts: new data from experiments with Ir10Pt90 alloys. *Geochimica et Cosmochimica Acta* **57**, 481–485.

Borisov, A. & Palme, H. (1997). Experimental determination of the solubility of platinum in silicate melts. *Geochimica et Cosmochimica Acta* **61**, 705–716.

Borisov, A. & Palme, H. (2000). Solubility of noble metals in Fe-containing silicate melts as derived from experiments in Fe free systems. *American Mineralogist* **85**, 1665–1673.

Borisov, A. & Walker, R. J. (2000). Os solubility in silicate melts: New efforts and results. *American Mineralogist* **85**, 912–917.

Borisov, A., Palme, H. & Spettel, B. (1994). Solubility of palladium in silicate melts: implications for core formation in the Earth. *Geochimica et Cosmochimica Acta* **58**, 705–716.

Boudreau, A. E. & Meurer, W. P. (1999). Chromatographic separation of the platinum group elements, gold, base metals and sulfur during degassing of a compacted and solidifying igneous crystal pile. *Contributions to Mineralogy and Petrology* **134**, 174–185.

Brenan, J. M. & Andrews, D. (2001). High temperature stability of laurite and Ru–Os–Ir alloy and their role in PGE fractionation in mafic magmas. *Canadian Mineralogist* **39**, 341–360.

Brenan, J. M., McDonough, W. F. & Ash, R. (2005). An experimental study of the solubility and partitioning of iridium, osmium and gold between olivine and silicate melt. *Earth and Planetary Science Letters* **237**, 855–872.

Capobianco, C. H., Hervig, R. L. & Drake, M. (1994). Experiments on crystal/liquid partitioning of Ru, Rh and Pd for magnetite and hematite solid solutions crystallised from silicate melt. *Chemical Geology* **113**, 23–43.

Choi, E. (2004). Multicomponent diffusion in the system K_2O–Na_2O–CaO–FeO–MgO–TiO_2–P_2O_5–Al_2O_3–SiO_2. M.Sc. thesis, University of Toronto.

Crank, J. (1975). *The Mathematics of Diffusion*. Oxford: Clarendon Press.

Eggins, S. M., Kinsley, L. P. J. & Shelleyet, J. M. M. (1998). Deposition and element fractionation processes during atmospheric pressure laser sampling for analysis by ICPMS. *Applied Surface Science* **127–129**, 278–286.

Ertel, W., O'Neill, H. St. C., Sylvester, P. J. & Dingwell, D. B. (1999). Solubilities of Pt and Rh in haplobasaltic silicate melt at 1300°C. *Geochimica et Cosmochimica Acta* **63**, 2439–2449.

Farges, F., Neuville, D. R. & Brown, G. E. (1999). Structural investigation of platinum solubility in silicate glasses. *American Mineralogist* **84**, 1562–1568.

Fleet, M. E. & Stone, W. E. (1991). Partitioning of platinum-group elements in the Fe–Ni–S system and their fractionation in nature. *Geochimica et Cosmochimica Acta* **55**, 245–253.

Fortenfant, S. S., Gunther, D., Dingwell, D. B. & Rubie, D. C. (2003). Temperature dependence of Pt and Rh solubilities in a haplobasaltic melt. *Geochimica et Cosmochimica Acta* **67**, 123–131.

Fortenfant, S. S., Dingwell, D. B., Ertel-Ingrisch, W., Capmas, F., Birk, J. L. & Dalpe, C. (2006). Oxygen fugacity dependence of Os solubility in haplobasaltic melt. *Geochimica et Cosmochimica Acta* **70**, 742–756.

Garuti, G., Zaccarini, M. & Economou-Eliopoulos, M. (1999). Paragenesis and composition of laurite from chromitites of Othrys (Greece): implications for Os–Ru fractionation in ophiolitic upper mantle of the Balkan Peninsula. *Mineralium Deposita* **34**, 312–319.

Gervilla, F. & Kojonen, K. (2002). The platinum-group minerals in the upper section of the Keivitsansarvi Ni–Cu–PGE deposit, northern, Finland. *Canadian Mineralogist* **40**, 377–394.

Ghiorso, M. S. & Sack, R. O. (1995). Chemical mass-transfer in magmatic processes 4. A revised and internally consistent thermodynamic model for the interpolation and extrapolation of liquid–solid equilibria in magmatic systems at elevated temperatures and pressures. *Contributions to Mineralogy and Petrology* **119**, 197–212.

Gijbels, R. H., Millard, H. T., Jr, Desborough, G. A. & Bartel, A. J. (1974). Osmium, ruthenium, iridium, and uranium in silicates and chromite from the eastern Bushveld complex, South Africa. *Geochimica et Cosmochimica Acta* **38**, 319–337.

Harmer, R. E. & Sharpe, M. R. (1985). Field relations and strontium isotope systematics of the marginal rocks of the eastern Bushveld complex. *Economic Geology* **80**, 813–837.

Hiemstra, S. A. (1979). The role of collectors in the formation of the platinum deposits in the Bushveld Complex. *Canadian Mineralogist* **17**, 469–482.

Hogg, A. J., Fawcett, J. J., Gittins, J. & Gorton, M. P. (1989). Cyclical variation in composition in continental tholeiites of East Greenland. *Canadian Journal of Earth Sciences* **26**, 534–543.

Irvine, T. N. (1977). Origin of chromitite layers in the Muskox intrusion and other stratiform intrusions: A new interpretation. *Geology* **5**, 273–277.

Irvine, T. N., Keith, D. W. & Todd, S. G. (1983). The J-M platinum–palladium reef of the Stillwater complex, Montana 2. Origin by double diffusive convective magma mixing and implications for the Bushveld complex. *Economic Geology* **78**, 1287–1334.

Kessel, R., Becket, J. R. & Stolper, E. M. (2001). Thermodynamic properties of the Pt–Fe system. *American Mineralogist* **86**, 1003–1014.

Kress, V. C. & Carmichael, I. S. E. (1991). The compressibility of silicate liquids containing Fe_2O_3 and the effect of composition, temperature, oxygen fugacity and pressure on their redox states. *Contributions to Mineralogy and Petrology* **108**, 82–92.

Legendre, O. & Agué, T. (1986). Mineralogy of Platinum-group mineral inclusions in chromitites from different ophiolitic complexes. In: Gallagher, M. J., Ixer, R. A., Neary, C. R. & Prichard, H. M. (eds) *Metallogeny of the Basic and Ultrabasic Rocks*. London: Institute of Mining and Metallurgy, pp. 361–375.

Liang, Y. (1999). Diffusive dissolution in ternary systems: Analysis with applications to quartz and quartzite dissolution in molten silicates. *Geochimica et Cosmochimica Acta* **63**, 3983–3995.

Liermann, H. P. & Ganguly, J. (2002). Diffusion kinetics of Fe^{2+} and Mg in aluminous spinel: Experimental determination and applications. *Geochimica et Cosmochimica Acta* **66**, 2903–2913.

Maier, W. D. & Barnes, S.-J. (1999). Platinum-group elements in silicate rocks of the Lower, Critical and Main zones at Union Section, Western Bushveld Complex. *Journal of Petrology* **40**, 1647–1671.

Maier, W. D., Barnes, S.-J., Gartz, V. & Andrews, G. (2003). Pt–Pd reefs in magnetitites of the Stella intrusion, South Africa: a world of new PGE exploration opportunities. *Geology* **31**, 885–888.

Malkovich, R. Sh. (2000). Diffusion in a composite medium for arbitrary initial distribution of concentration. *Solid State Phenomena* **72**, 255–260.

Mathez, E. A. (1995). Magmatic metasomatism and formation of the Merensky Reef, Bushveld complex. *Contributions to Mineralogy and Petrology* **119**, 277–286.

Merkle, R. K. W. (1992). Platinum-group elements in the middle group of chromitite layers at Marikana, western Bushveld Complex: indications for collection mechanisms and postmagmatic modification. *Canadian Journal of Earth Sciences* **29**, 209–221.

Mondal, S. K. & Mathez, E. A. (2007). Origin of the UG2 chromitite layer, Bushveld Complex. *Journal of Petrology* **48**, 495–510.

Mungall, J. (2001). Empirical models relating viscosity and tracer diffusion in magmatic silicate melts. *Geochimica et Cosmochimica Acta* **66**, 125–143.

Mungall, J. (2002). A model for co-precipitation of platinum group minerals with chromite from silicate melts. In: *Abstracts, 9th International Platinum Symposium, July, Stillwater, USA*. Available at http://www.nicholas.duke.edu/people/faculty/boudreau/IPS_Abstracts.htm.

Murck, B. W. & Campbell, I. H. (1986). The effects of temperature, oxygen fugacity and melt composition on the behavior of chromium in basic and ultrabasic melts. *Geochimica et Cosmochimica Acta* **50**, 1871–1887.

Naldrett, A. J. & Lehmann, J. (1988). Spinel non-stoichiometry as the explanation for Ni-, Cu-, and PGE-enriched sulphides in chromitites. In: Prichard, H. M., Potts, P. J., Bowles, J. F. W. & Cribb, S. J. (eds) *Geo-Platinum 87*. Barking: Elsevier Applied Science, pp. 93–109.

O'Neill, H. St. C., Dingwell, D. B., Borisov, A., Spettle, B. & Palme, H. (1995). Experimental petrochemistry of some high siderophile elements at high temperatures and some implications for core formation and the mantle's early history. *Chemical Geology* **120**, 255–273.

O'Neill, H. St. C., Berry, A. J., McCammon, C. C., Jayassuriya, K., Campbell, S. J. & Foran, G. (2006). An experimental determination of the effect of pressure on the $Fe^{3+}/\sum Fe$ ratio of anhydrous silicate melt to 3·0 GPa. *American Mineralogist* **91**, 404–412.

Parkinson, I. J. & Arculus, R. J. (1999). The redox state of subduction zones: insights from arc-peridotites. *Chemical Geology* **160**, 409–423.

Peck, D. C., Keays, R. R. & Ford, R. J. (1992). Direct crystallisation of refractory platinum group element alloys from boninitic magmas: Evidence from western Tasmania. *Australian Journal of Earth Sciences* **39**, 373–387.

Peregoedova, A., Barnes, S. J. & Baker, D. R. (2004). The formation of Pt–Ir alloys and Cu–Pd rich sulfide melts by partial desulfurization of Fe–Ni–Cu sulfides: results of experiments and implications for natural systems. *Chemical Geology* **208**, 247–264.

Puchtel, I. S. & Humayen, M. (2001). Platinum group element fractionation in a komatiitic basalt lava lake. *Geochimica et Cosmochimica Acta* **65**, 2979–2994.

Puchtel, I. S., Humayen, M., Campbell, A. J., Sproule, R. & Lesher, C. M. (2004). Platinum group element geochemistry of komatiites from the Alexo and Pyke hill areas, Ontario, Canada. *Geochimica et Cosmochimica Acta* **68**, 1361–1383.

Roeder, P. L. & Reynolds, I. (1991). Crystallisation of chromite and chromium solubility in basaltic melts. *Journal of Petrology* **32**, 909–934.

Roeder, P. L., Poustovetov, A. & Oskarsson, N. (2001). Growth forms and composition of chromian spinel in MORB magma: Diffusion-controlled crystallization of chromian spinel. *Canadian Mineralogist* **39**, 397–416.

Sattari, P., Brenan, M. B., Horn, I. & McDonough, W. F. (2002). Experimental constraints on the sulfide– and chromite–silicate melt partitioning behaviour of rhenium and the platinum group elements. *Economic Geology* **97**, 385–398.

Schreiber, H. D. & Haskin, L. A. (1976). Chromium in basalts: Experimental determination of redox states and partitioning among synthetic silicate phases. *Proceedings of the 7th Lunar Science Conference. Geochimica et Cosmochimica Acta Supplement* **7**, 1221–1259.

Sun, R. (1958). Diffusion of cobalt and chromium in chromite spinel. *Journal of Chemical Physics* **28**, 290–293.

Talkington, R. W. & Lipin, B. R. (1986). Platinum group minerals in the chromite seams of the Stillwater Complex, Montana. *Economic Geology* **81**, 1179–1186.

Tredoux, M., Lindsay, N. M., Davies, G. & Mcdonald, I. (1995). The fractionation of platinum-group elements in magmatic systems, with the suggestion of a novel causal mechanism. *South African Journal of Geology* **98**, 157–167.

Tylkina, M. A., Polyakova, V. P. & Savitskii, E. M. (1962). The Ru–Os phase diagram. *Russian Journal of Inorganic Chemistry* **7**, 754–755.

Zaccarini, F., Garuti, G. & Cawthorn, R. G. (2002). Platinum-group minerals in chromitite xenoliths from Onverwacht and Tweefontein ultramafic pipes, eastern Bushveld Complex, South Africa. *Canadian Mineralogist* **40**, 481–497.